NURETH14-464

IMPROVEMENT OF IMAGE PROCESSING ALGORITHMS FOR ANNULAR FLOW

Wesley Kokomoor and DuWayne Schubring

University of Florida
202 Nuclear Science Building
P.O. Box 118300
Gainesville FL 32611-8300
wesleyk@ufl.edu; dlschubring@ufl.edu

Abstract

Annular flow occurs in a wide range of industrial heat-transfer equipment, including the top of a BWR core, in the steam generator of a PWR, and in postulated accident scenarios including critical heat flux (CHF) by dryout. The modeling of annular flow often requires information regarding the average thickness of liquid film at the periphery of the flow channel as a measurement of film roughness (film roughness concept). More recently, two-region modeling efforts require wave intermittency as a measurement of disturbance wave (as opposed to base film thickness) contribution to gas-to-liquid momentum transfer and pressure loss.

The present work focuses on the characterization of film behaviors in annular flow using quantitative visualization. The data reduction codes for planar laser-induced flourescence (PLIF) imaging and backlit quartz tube imaging have been further developed to improve measurement accuracy. Film thickness distribution (base film and wave), disturbance wave length, and wave intermittency estimates have been updated and applied to a recent two-region annular flow model. Outputs of average film thickness, pressure gradient, and average wave velocity have been modeled with mean absolute errors of 8.70%, 17.42%, and 19.14%, respectively.

1. Introduction

Annular two-phase gas-liquid flow is characterized by a core of fast moving gas surrounded by a thin film of liquid. This regime occurs through a wide range of gas and liquid flow rates, is often observed in the core of boiling water reactors, and can be the predominant regime in steam generators. Annular flow is also the final stage in channel boiling before gas-droplet flow occurs in critical heat flux (CHF) by dryout (postulated BWR accident scenario).

Liquid transport in annular flow occurs at two locations: in the liquid film at the periphery of the channel and by droplets traveling through the gas core (entrainment). The liquid film has been observed by Hewitt [1] as a combination of thin, smooth base film and relatively thick, rough disturbance waves. The presence of disturbance waves in annular flow has been recognized and studied in some detail, including review papers by Azzopardi in 1986 [2] and 1997 [3].

Most annular flow modeling uses the film roughness concept discussed by Hewitt and Hall Taylor [4], wherein the roughness in the liquid film enhances friction at the gas-liquid interface. Additionally, recent attempts at modeling use a two-zone approach where the base film zone and disturbance wave zone are modeled separately (Hurlburt *et al.* [5], Schubring and Shedd [6]).

The interfacial friction enhancement from the liquid film has been expressed as various functions of average film thickness in the literature (Wallis [7], Asali *et al.* [8], Owen and Hewitt [9]). Most measurements of average film thickness have been taken using conductance probes – such as those by Brown [10], Fossa [11], and Fore *et al.* [12] – that measure film thickness by electrical conductivity through a known channel distance. Conductance measurements have many drawbacks, including instrumentation that is often intrusive to the fluid flow, and limited ability to distinguish between base film and disturbance waves.

Ideally, film roughness would be linked to the distribution of instantaneous, local film height. A method for measuring film thickness from cross-sectional images of liquid film (base and wave) has been developed by Schubring *et al.* [13]. These planar laser-induced flourescence (PLIF) measurements not only allow for point measurements of film thickness, but also simultaneous measurements of base film and waves. The current work includes futher development of the original data reduction code created for those measurements.

Two-zone models require wave intermittency (INT_w) to link the base and wave zones, defined as the fraction of time a disturbance wave is present at a location on the liquid film (versus a location along the tube axis). Previous definitions of INT_w assume that a disturbance wave is symmetric about the tube axis and that an axial location is sufficient. Disturbance wave length (L_{wave}) and INT_w measurements have been performed by Schubring *et al.* [14] using high-speed video of a back-lit quartz tube. The data reduction code for those measurements has been adjusted in the current work to accommodate asymmetry in disturbance waves.

The observations from PLIF and high-speed video algorithm changes have been applied to the two-zone model of Schubring and Shedd [6]. Modifications to the model include roughness estimates for each zone, revised correlations for INT_w and wave length (L_{wave}) , additional correlation for wave-to-base film height ratio, and updates to base and wave zone friction estimates.

2. PLIF Edge Detection Modifications

PLIF processing uses MATLAB code in three sections, as outlined in the original work of Schubring *et al.* [13]: image processing, outlier-removal, and data processing. The expected shape of the liquid edge is a smooth, continuous, unbroken line through the length of the image.

2.1 Image Processing

Some obstacles overcome in the liquid edge-finding routine include image contrast, single-pixel image noise, bubbles in the gas-liquid interface, and out-of-plane features including droplets near the interface. The modifications to the original code are discussed below, shown in order of operation.

Crop The image is cropped to a specified width to reduce the image processing time and reduce the impact of droplets at the outer range of the images. The initial crop widths are a function of the gas flow rates, based on the maximum observed film thickness for each liquid flow: 2000 μ m for 800 L min⁻¹, 1500 μ m for 1000 L min⁻¹, 1250 μ m for 1200 L min⁻¹, 1100 μ m for 1400 L min⁻¹, 800 μ m for 1600 L min⁻¹.

Contrast Adjustment The raw images are initially too dark for viewing by the human eye. The pixel range of the images is adjusted using a MATLAB function, imadjust. The main operation in imadjust is shown in Equation 1 where J is the output image, I is the input image, and subscripts min, max, and n represent the minimum, maximum, and current pixel value in the image, respectively. The exponential weighting factor, γ , has been set to 1.5 to wieght the output towards the lower pixel values and help reduce blur in the gas core.

$$J_n = J_{min} + (J_{max} - J_{min}) \left[\frac{(I_n - I_{min})}{(I_{max} - I_{min})} \right]^{\gamma}$$
 (1)

Stretch The adjusted image is then enhanced a second time by applying a row-by-row linear stretch of the pixel values, creating a better defined edge for low contrast regions. The original code over-stretched and blurred some regions of the film, so a stretching threshold is implemented in the current version. A minimum-to-maximum pixel difference of 74 (out of 255) is required for a row before it is linearly stretched.

The newly stretched image $(Temp_{str})$ is then added to the previous adjusted image (Adjusted) as in Equation 2. The weighting factor for the addition was determined by visual inspection to reduce the axial noise created by the stretching process.

$$Stretched = 0.8 \times Temp_{str} + 0.2 \times Adjusted$$
 (2)

Opening / Closing A morphological opening and closing is applied to the stretched image with built-in MATLAB functions imopen and imclose to reduce the effects of small-scale defects in the edge. The first time through the processing, a disk of radius 3 pixels is used. All other iterations, which contain edge data and updated image size, use a variable system of morphological disk radii described in Equation 5 (units of pixels).

An image can be subject to three different open/close radii (R_{oc}) depending on the distance from the channel wall (y) and the array of edge locations (Edge). The parameters C_1 and C_2 are distances from the channel wall where the morphological radius changes, and are based on the height and roughness (standard deviation) of the liquid edge. This system was developed since higher edge locations (e.g., waves) show more chaotic edge behavior, larger bubbles, and more edge defects. The larger radii are more effective at smoothing this behavior.

$$C_1 = \overline{Edge} + 2 \times s(Edge) \tag{3}$$

$$C_2 = 1.6C_1 (4)$$

$$R_{oc}(z) = \begin{cases} 1 & \text{for } y(z) \le C_1 \\ 6 & \text{for } C_1 < y(z) \le C_2 \\ 13 & \text{for } C_2 < y(z) \end{cases}$$
 (5)

Film Threshold The binary threshold for the current code has been decreased significantly from the original due to new contrasting methods. The film threshold of 175 (out of 255) was reduced to 85.

Edge Iteration A system was developed to compare the disagreements in the edge recordings on the basis of edge continuity. The recorded values that produce a more continuous liquid edge – not representing entrained droplets or dispersed bubbles – are accepted as the final values based on local calculations of chaos and standard deviation. The final edge vector undergoes a one-dimensional median filter (radius of 11 pixels) to remove any remaining pixel noise.

Bubble Elimination A bubble reduction algorithm is employed for smaller defects caused by bubbles in the interface. Edge perturbations between 0 and 200 μ m long, with a depression of at least 15 μ m, are recorded as bubble defects. Once located, the bubble section is fixed by linearly interpolating between the outer pixels.

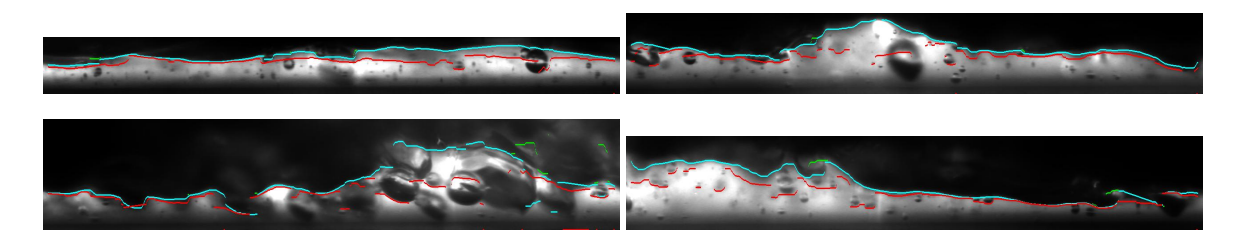


Figure 1: Example processed PLIF images. $U_{sg} = 45.0 \,\mathrm{m \, s^{-1}}$, $U_{sl} = 6.3 \,\mathrm{cm \, s^{-1}}$. Red line shows original results, light blue line shows current results.

2.2 Outlier Removal

Certain features of the liquid film can cause errors in the recorded liquid edge. Some also cause failure in the edge finding routine. It is preferable to locate and reject such "outlier" images. Any measurement of standard deviation or chaos is not sufficient grounds for image rejection – highly chaotic edge vectors have occasionally been observed to be accurate. For this reason, a graphical user interface (GUI) was produced using MATLAB to aid in the visual identification of outliers.

The GUI loads one set of processed flow data at a time and calculates the mean and standard deviation of all edge values. A list of potential outliers is produced for which the mean of the edge vector lies outside of a critical range. The default critical range is calculated as 2 standard deviations away from the mean, but can be modified in the GUI. This criterion primarily locates edge vectors that are uncharacteristically high. A similar criterion is evaluated using a metric for erratic edges. From this list, the user selects an image, views the image and edge data, and determines whether it qualifies as an outlier. Images were only rejected if the recorded edge represented the film incorrectly as a result of the following:

Core liquid Some images show droplets or larger sections of liquid traveling through the core. This is often much farther from the wall than the liquid film and can skew the data if detected. Even if detected, liquid in the core has been observed to affect, at most, 10% of an image. Due to the disparity in the recorded values, any falsely detected liquid in the core that affects more than 5% of a recorded edge (by visual estimation) is removed.

Out-of-plane features Some features, unidentifiable as part of the liquid film, show up in images as large, blurry patches. Out-of-plane features occur in large sections, often affecting over 15% of a recorded edge. All of the images with this type of issue are rejected.

Erratic film sections Some images show a liquid edge that is extremely erratic and not well characterized by the image processing. This can be caused by several mechanisms, such as a large concentration of bubbles at the interface, a large wave with liquid tearing from the surface, or the rolling/breaking of a large wave. Errors of this type occur at varying levels of severity (disparity between the recorded edge and the true edge location) and are rejected on a case-by-case basis.

Some example images that were selected as outliers have been shown in Figure 2. Typically, between 1% and 5% of the total images in a flow condition are selected as outliers. An array is created by the GUI that indicates which images were selected, later used in the data analysis.

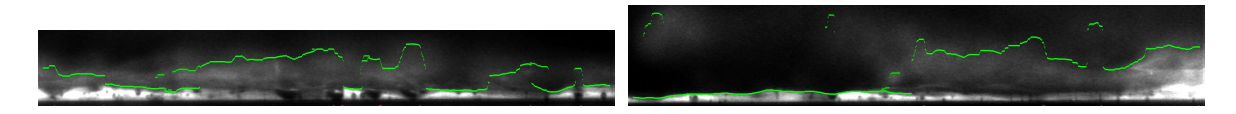


Figure 2: Example rejected PLIF images. $U_{sl} = 21.1 \text{ cm s}^{-1}$. $U_{sg} = (left) 66.9 \text{ m s}^{-1}$, $(right) 56.5 \text{ m s}^{-1}$.

3. High-Speed Wave Video Modifications

High-speed videos of 65 vertical annular flow conditions were acquired and analyzed in the work of Schubring, Shedd and Hurlburt [14] and in the dissertation of Schubring [15]. The two major objectives of the studies were to:

- Demonstrate the use of high-speed video to estimate the velocities, lengths, and temporal spacings of individual waves.
- Use these individual wave measurements to develop average velocites, lengths, frequencies and intermittencies of disturbance waves as functions of gas and liquid flow rates.

The current work represents improved wave length measurements to address the circumferential asymmetry of disturbance waves. Two measurement techniques have been applied to estimate the length of disturbance waves, a single-section measurement (original code) and a multi-section measurement (current code). A schematic of the two measurement techniques is shown in Figure 3, where L_1 represents the original estimate and L_2 is the current estimate. The single-section method proceeds by locating the center of the wave (darkest section), then scanning in both directions to find the forward and rear edges of the wave. The wave is then recorded as the difference between the two edge recordings.

The multi-section method proceeds by identifying the center of the wave in the same manner as the original code. The image is then split into four equal sections (Img(sec), sec = 1 through 4) along the tube width. Each section is then averaged along its width to produce avedarki(sec), then normalized by the time-independent average for the entire flow condition (avedarkX) to produce ddarki(sec), shown in Equation 6.

$$ddarki(sec) = \overline{Img(sec)} - avedarkX \tag{6}$$

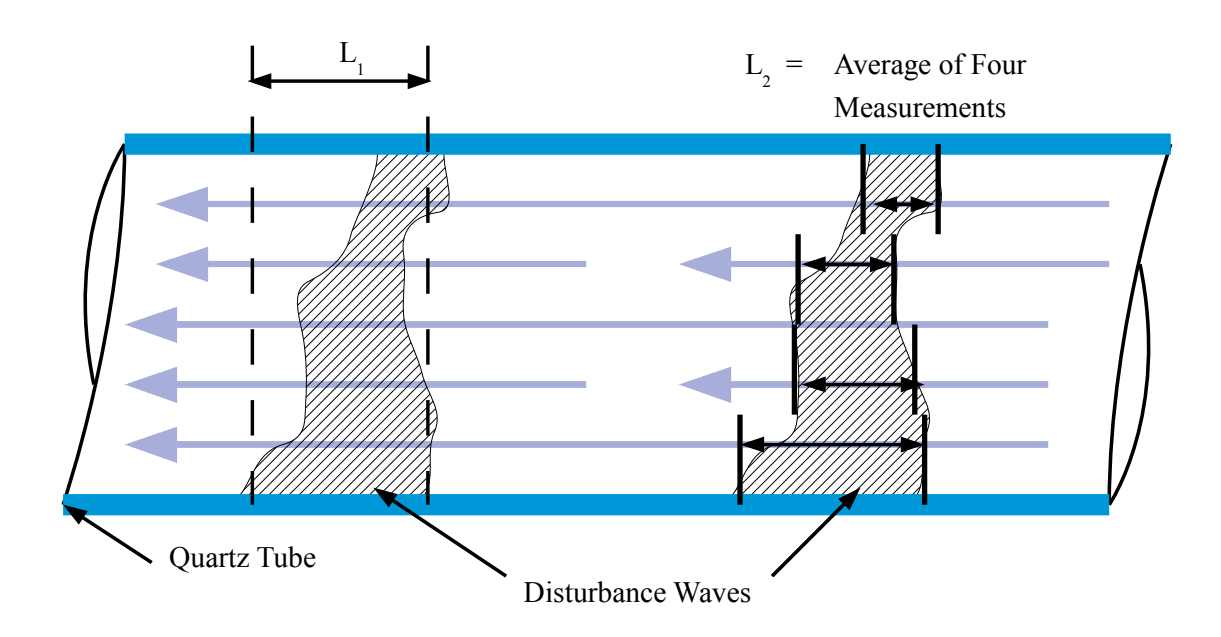


Figure 3: Schematic of the new (left) and old (right) measurement techniques used to estimate wave length.

A threshold is then applied to ddarki(sec) to locate the passing wave, producing ddarkiBW(sec). Due to the varying level of contrast in each image, the wave threshold, $Th_{wave}(sec)$, is a function of the average and standard devation of each section, shown in Equation 7.

$$Th_{wave}(sec) = \overline{ddarki(sec)} + k_{sec}s(ddarki(sec)) \tag{7}$$

$$ddarkiBW(sec) = ddarki(sec) > Th_{wave}(sec)$$
(8)

The variation in contrast also appeared to be a strong function of liquid flow rate. The standard deviation multiplier, k_{sec} , is linearly altered between as a function of Q_l shown in Equation 9. The multiplier extremes, $k_{sec,max}$ and $k_{sec,min}$, are set to -0.45 and -1.00, respectively.

$$k_{sec} = k_{sec,min} + (Q_l - Q_{l,min}) \left[\frac{k_{sec,max} - k_{sec,min}}{Q_{l,max} - Q_{l,min}} \right]$$
(9)

Starting at the center of the wave (recorded earlier) each ddarki(sec) array is searched left (towards the front of the wave) and right (towards the back of the wave) to find the front and back wave edges. The wave length for the image (L_{wave}) is recorded as the average of all four wave section measurements (L_{sec}) and converted to a physical scale. The wave intermittency for the flow condition is then calculated as:

$$INT_w = \frac{L_{wave} f_{wave}}{v_{wave}} \tag{10}$$

4. Global Model Modifications

The global model of Schubring and Shedd [6] has been modified based on results of the discussed algorithm modifications. The optimization of the model proceeds by first updating the film behavior correla-

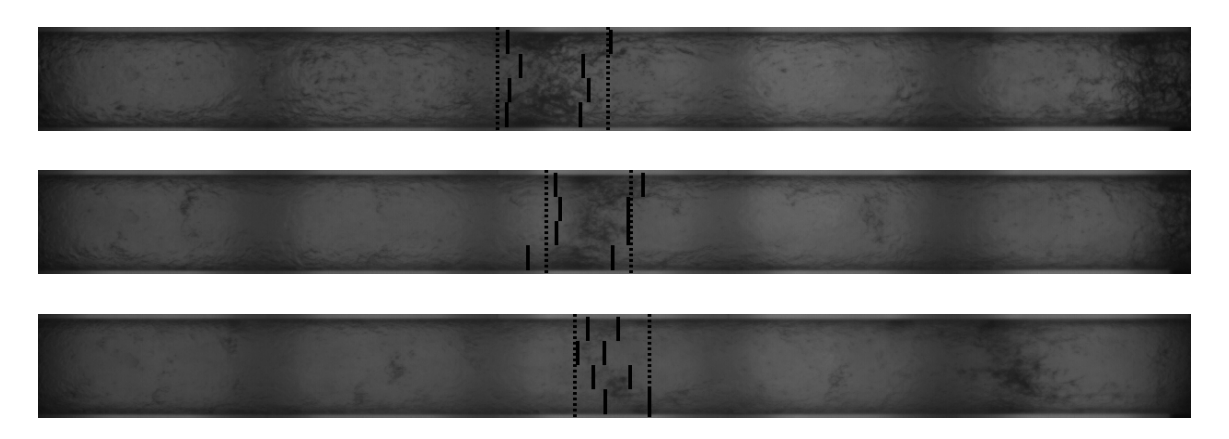


Figure 4: Example wavelength comparison images for varying gas velocities, $U_{sl} = 7.8 \text{ cm s}^{-1}$. U_{sg} (top to bottom) = 32 m s⁻¹, 50 m s⁻¹, 70 m s⁻¹

tions developed in the current work. The second step is determining which parameters in the model can be adjusted to improve agreement with data and to more accurately reflect the physics of annular flow.

The metrics of optimization for this work are the errors between correlated parameters and measured outputs, which vary depending on the measurement test section. For the FEP test section (used for PLIF film measurement), average film thickness (δ), base film thickness (δ), and wave height (δ_{wave}) data are available. For the quartz test section, pressure gradient (dP/dz) and disturbance wave velocity (v_{wave}) data are available.

4.1 Re-Correlated Film Behavior

The updated PLIF wave length measurement techniques have resulted in changes to film behavior approximations in the model. The specific contributions of these adjustments to the global model are described by visualization method.

4.1.1 PLIF Observations

The Schubring and Shedd model relies on observations of roughness in the base zone, roughness in the wave zone, and an approximation of wave-to-base film height ratio. The following observations have been made in the current work that update those observations in the model:

Base Film Roughness The base film roughness is calculated in the current work as twice standard deviation of base film data (same as the original work) and is used two ways in the model:

- 1. In the roughness friction factor from Hurlburt et al..
- 2. To approximate the fraction of base film that travels with a linear profile (linear fraction, LF_{base}).

The original observation agrees well with the current work, demonstrating a constant relative roughness of 0.6 and a LF_{base} of 0.7.

Wave Height Roughness The wave roughness is calculated as twice the standard deviation of wave data and is applied in the roughness friction factor. The roughness in the wave zone has been observed in the current work as 60% of δ_{wave} (an increase from the original observation of 40%).

Wave-to-Base Ratio The original work estimated mean wave height as 2 times the mean base height, which did not explain some low liquid flow behaviors. The current work shows that the ratio is actually a function of gas and liquid flow rate. An empirical correlation was developed to express this ratio as a function of flow quality:

$$\frac{\delta_{wave}}{\delta_{base}} = 1.86x^{-0.18} \tag{11}$$

4.1.2 High-Speed Video Observations

The updated wave length (L_{wave}) measurement resulted in different observations of wave length and wave intermittency (INT_w) than the original work.

Wave Length Observations The wave length distributions in the current work show generally shorter values for L_{wave} than previously observed. The correlation for L_{wave} developed by Schubring *et al.* [14] has been re-optimized to fit the new measurements:

$$L_{wave,KS} = 0.43 \frac{D}{x^{0.63}} \tag{12}$$

Wave Intermittency Observations INT_w is closely linked to L_{wave} . The correlation for INT_w developed by Schubring *et al.* [14] has been re-optimized to fit the new measurements:

$$INT_{w,KS} = 0.07 + \frac{Re_l}{49000} \tag{13}$$

4.2 Model Adjustments

Some parameters in the Schubring and Shedd model are purely empirical. The goal of a global model is to describe annular flow from physical principles. The calculation of wave shear from sharp base-wave transitions, $\tau_{i,wave,trans}$, is one violation of this goal by employing a purely empirical factor of 2. This parameter has been removed, lowering the contribution of transition shear:

$$\tau_{i,wave,trans} = \frac{\rho_{core} \overline{U_{g,trans}}^2 (\delta_{wave} - \delta_{base})}{L_{wave}}$$
(14)

The base and wave zone sub-models both use the rough tube friction factor suggested by Hurlburt *et al.* [5] the empirical constants $c_{B,base}$ and $c_{B,wave}$. These constants appear in the equations in a natural logarithm; setting them to 1.0 removes them from the equations:

$$C_{f,i,base} = 0.58^2 \left[-\frac{\ln \hat{\epsilon}_{base}}{(\hat{\epsilon}_{base} - 1)^2} + 1.05 + \frac{1}{2} \frac{\hat{\epsilon}_{base} + 1}{\hat{\epsilon}_{base} - 1} \right]^{-2}$$
(15)

$$C_{f,i,wave} = 0.58^2 \left[-\frac{\ln \hat{\epsilon}_{wave}}{(\hat{\epsilon}_{wave} - 1)^2} + 1.05 + \frac{1}{2} \frac{\hat{\epsilon}_{wave} + 1}{\hat{\epsilon}_{wave} - 1} \right]^{-2}$$
(16)

The prediction of film thickness (both zones) and wave velocity is very sensitive to the friction correlation and the roughness enhancement factor, ϕ_{RR} . The equation for ϕ_{RR} has been adjusted from its original form to the following:

$$\phi_{RR} = 2.18x^{-0.1} \tag{17}$$

The original model observed a poor correlation of wave velocity outputs for series of constant liquid flow, which increased too quickly with increasing gas flow rate. This can be attributed to an over-prediction of wave velocity by the Universal Velocity Profile. To remedy this, the top 30% of the film $VF_{wave}=0.3$) is assumed to travel at a coherent velocity – the wave velocity:

$$U_{l.i.wave}^{+} = 5.5 + 2.5 \ln \left((1 - V F_{wave}) \delta_{wave}^{+} \right)$$
 (18)

$$U_{l,i,wave} = U_{l,i,wave}^{+} u_{wave}^{\star} \tag{19}$$

$$1 - VF_{wave} = 0.7 \tag{20}$$

This matches the assumed physics in the base film zone, as well as what is observed from imaging.

4.3 Results

The previously discussed expressions for wave-to-base ratio, disturbance wave length, and wave intermittency performed with a mean absolute error of 6.74%, 15.91%, and 9.47% respectively (shown in Table I).

Table I: Error calculations for global model correlations.

Correlated Parameter	Error (%)	MAE (%)	RMS (%)
$\delta_{wave}/\delta_{base}$	-0.25	6.74	8.13
$L_{wave,KS}$	-1.58	15.91	20.50
$INT_{w,KS}$	-1.10	9.47	12.13

The original model was developed first with consideration of the vertical FEP tube flow conditions, used primarily for the PLIF film thickness measurements. The separation between base and wave zones has been performed using the INT_w values from disturbance wave visualization. Average values for δ , δ_{base} , and δ_{wave} are available for each flow condition from PLIF results and show mean absolute errors of 8.70%, 8.93%, and 9.82% respectively. Flow conditions studied in the quartz tube allow for direct comparisons of modeled results to pressure gradient and wave velocity, and show errors of 17.42% and 19.14%, respectively.

Table II: Performance of present global model.

Correlated Parameter	Mean Error [%]	MAE [%]	RMS [%]
δ	-0.10	8.70	11.11
δ_{base}	0.17	8.93	11.49
δ_{wave}	0.42	9.82	14.31
dP/dz	0.45	17.42	23.22
v_{wave}	10.88	19.14	20.99

5. Conclusion

The data reduction codes for PLIF liquid edge identification and high-speed wave video have been modified to improve measurement accuracy. The two-region global model of Schubring and Shedd [6] has been updated with film roughness observations and revised correlations for wave-to-base ratio, wave length, and wave intermittency. The resulting performances for individual flow behaviors are reasonable, especially considering the low requirements for model inputs.

References

- 1. G. F. Hewitt, S. Jayanti, and C. B. Hope, Structure of thin liquid films in gas-liquid horizontal flow. *International Journal of Multiphase Flow.* **Vol. 16**, pp. 951–957 (1990).
- 2. B. J. Azzopardi, Disturbance wave frequencies, velocities and spacing in vertical annular two-phase flow. *Nuclear Engineering and Design.* **Vol. 92**, pp. 121–133 (1986).
- 3. B. J. Azzopardi, Drops in annular two-phase flow. *International Journal of Multiphase Flow*. **Vol. 23**, pp. 1–53 (1997).
- 4. G. F. Hewitt and N. S. Hall Taylor, Annular Two-Phase Flow. Pergamon Press, Oxford, UK (1970).
- 5. E. T. Hurlburt, L. B. Fore, and R. C. Bauer, A two zone interfacial shear stress and liquid film velocity model for vertical annular two-phase flow. Miami, FL, USA, Vol. 2, pp. 677–684 (2006).
- 6. D. Schubring and T. Shedd, A model for pressure loss, film thickness, and entrained fraction for gas-liquid annular flow. *International Journal of Heat and Fluid Flow In Press* (2011).
- 7. G. B. Wallis, One-dimensional Two-phase Flow. McGraw-Hill, Inc., New York, NY, USA (1969).
- 8. J. C. Asali, T. J. Hanratty, and P. Andreussi, Interfacial drag and film height for vertical annular flow. *AIChE Journal.* **Vol. 31**, pp. 895–902 (1985).

- 9. D. G. Owen and G. F. Hewitt, An improved annular two-phase flow model. The Hague, Netherlands, pp. 73–84 (1987).
- 10. R. C. Brown, P. Andruessi, and S. Zanelli, The use of wire probes for the measurement of liquid film thickness in annular gas-liquid flows. *The Canadian Journal of Chemical Engineering*. **Vol. 56**, pp. 754 757, Dec. 1978.
- 11. M. Fossa, Design and performance of a conductance probe for measuring the liquid fraction in two-phase gas-liquid flows. *Flow Measurement and Instrumentation*. **Vol. 9**, pp. 103–109 (1998).
- 12. L. B. Fore, S. G. Beus, and R. C. Bauer, Interfacial friction in gas-liquid annular flow: analogies to full and transition roughness. *International Journal of Multiphase Flow*. **Vol. 26**, pp. 1755–1769 (2000).
- 13. D. Schubring, A. C. Ashwood, T. A. Shedd, and E. T. Hurlburt, Planar laser-induced fluorescence (PLIF) measurements of liquid film thickness in annular flow. Part I: Methods and data. *International Journal of Multiphase Flow.* Vol. 36, pp. 815–824 (2010).
- 14. D. Schubring, T. A. Shedd, and E. T. Hurlburt, Studying disturbance waves in vertical annular flow with high-speed video. *International Journal of Multiphase Flow*. **Vol. 36**, pp. 385–396 (2010).
- 15. D. Schubring, *Behavior interrelationships in annular flow*. PhD thesis, University of Wisconsin-Madison, WI, USA (2009).